Microwave-Induced Structural Engineering and Pt Trapping in *6R*-TaS$_2$ for the Hydrogen Evolution Reaction

Leyla Najafi, Sebastiano Bellani,* Reinier Oropesa-Nuñez, Rosaria Brescia, Mirko Prato, Lea Pasquale, Cansunur Demirci, Filippo Drago, Beatriz Martín-García, Jan Luxa, Liberato Manna, Zdeněk Sofer, and Francesco Bonaccorso*

The nanoengineering of the structure of transition metal dichalcogenides (TMDs) is widely pursued to develop viable catalysts for the hydrogen evolution reaction (HER) alternative to the precious metallic ones. Metallic group-5 TMDs have been demonstrated to be effective catalysts for the HER in acidic media, making affordable real proton exchange membrane water electrolysers. Their key-plus relies on the fact that both their basal planes and edges are catalytically active for the HER. In this work, the *6R* phase of TaS$_2$ is "rediscovered" and engineered. A liquid-phase microwave treatment is used to modify the structural properties of the *6R*-TaS$_2$ nanoflakes produced by liquid-phase exfoliation. The fragmentation of the nanoflakes and their evolution from monocrystalline to partly polycrystalline structures improve the HER-activity, lowering the overpotential at cathodic current of 10 mA cm^{-2} from 0.377 to 0.119 V. Furthermore, *6R*-TaS$_2$ nanoflakes act as ideal support to firmly trap Pt species, which achieve a mass activity (MA) up 10 000 A g$_{Pt}^{-1}$ at overpotential of 50 mV (20 000 A g$_{Pt}^{-1}$ at overpotentials of 72 mV), representing a 20-fold increase of the MA of Pt measured for the Pt/C reference, and approaching the state-of-the-art of the Pt mass activity.

1. Introduction

The design of efficient electrocatalysts for water splitting reactions is crucial to unlock the "Hydrogen economy,"[1] the vision of using molecular hydrogen (H$_2$) as carbon-free fuel produced by renewable energy sources.[2] To embrace H$_2$ as game changer, academic research is struggling to develop advanced electrolysers, while reducing their investment and operational costs.[3] In this context, proton exchange membrane (PEM) water electrolysers overcome several operational drawbacks of commercial alkaline ones,[4] for example, low maximum achievable current density (between 200 and 400 mA cm^{-2}), low operating pressure (<30 bar), inefficient dynamic operation (acceptable part-load operation between 10 and 40% of the nominal load), and gas crossover phenomena (typical gas purity <99.9%).[3,5] Nonetheless, the costs and the scarcity of their most effective catalysts, for example, Pt-group elements for the hydrogen evolution reactions (HER) at the cathode,[6,7] and RuO$_2$/IrO$_2$ for the oxygen evolution reactions at the anode,[8,9] hinder massive commercial products.[10] To face the cost-related barriers of the PEM electrolysers, it is mandatory to search for alternative non-precious catalysts,[11,12] or at least to reduce the content of precious metals, while still maintaining the electrochemical

Dr. L. Najafi, Dr. S. Bellani, Dr. B. Martín-García, Dr. F. Bonaccorso
Graphene Labs
Istituto Italiano di Tecnologia
via Morego 30, Genova 16163, Italy
E-mail: sebastiano.bellani@iit.it; francesco.bonaccorso@iit.it

Dr. L. Najafi, Dr. S. Bellani, Dr. R. Oropesa-Nuñez, Dr. F. Bonaccorso
BeDimensional Spa.
via Albisola 121, Genova 16163, Italy

Dr. R. Oropesa-Nuñez
Department of Material Science and Engineering
Solid State Physics
Uppsala University
Uppsala 75103, Sweden

Dr. R. Brescia
Electron Microscopy Facility
Istituto Italiano di Tecnologia
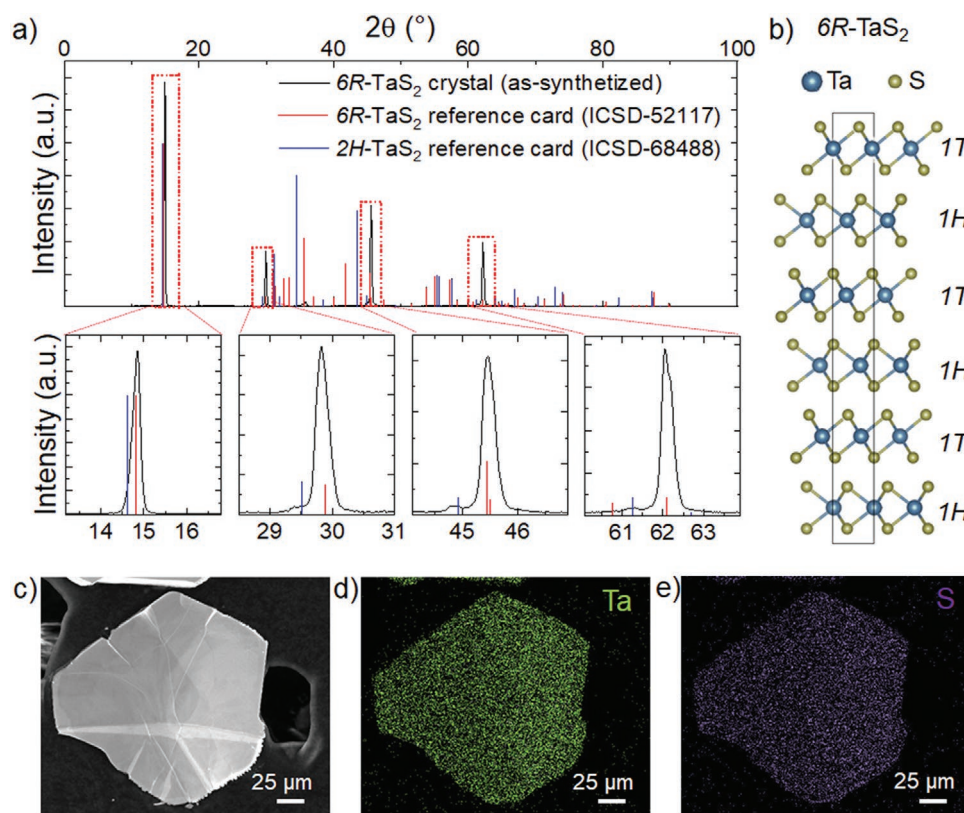Via Morego 30, Genova 16163, Italy

Dr. M. Prato, Dr. L. Pasquale
Materials Characterization Facility
Istituto Italiano di Tecnologia
via Morego 30, Genova 16163, Italy

Dr. C. Demirci, F. Drago, Dr. L. Manna
NanoChemistry
Istituto Italiano di Tecnologia
via Morego 30, Genova 16163, Italy

Dr. J. Luxa, Prof. Z. Sofer
Department of Inorganic Chemistry
University of Chemistry and Technology Prague
Technická 5, Prague 6 16628, Czech Republic

performance of the electrodes. This means to maximize the surface catalytic activity and/or surface-to-bulk atomic ratio of the catalysts.[13] Recently, 2D transition metal dichalcogenides (TMDs) have been investigated as a catalytic model to perform the HER processes.[14] In particular, first-principle density functional theory (DFT) calculations[15,16] and experimental studies[16,17] revealed that the unsaturated edges of the semiconducting (2H) phase and the metallic (1T) phase of group-6 TMDs (e.g., MoS_2 and WS_2) are catalytically active for the HER. However, the inertness of the basal planes of their natural semiconducting phase (2H),[18] and the susceptibility of the electronic structure of their catalytic sites to the electrochemical environment,[19] result in insufficient current densities (typically ≤100 mA cm^{-2}) to be exploited in advanced electrolysers. Contrary to the group-6 TMDs, the metallic group-5 TMDs (e.g., TaS_2 and NbS_2) have been predicted to display both edges and basal planes as catalytic sites in their natural phases.[20–25] In agreement with these theoretical expectations, chemical vapor deposition (CVD)-synthesized $2H$-TaS_2 and $2H$-NbS_2 nanoplatelets displayed an overpotential at cathodic current density of 10 mA cm^{-2} (η_{10}) of ≈50–60 mV with a catalyst loading in the order of tens µg cm^{-2},[20] indicating a per-site HER-activity (or mass activity—MA—) similar to that of Pt.[6,7] Similar results have also been achieved by another metallic polytype group-5 TMDs, namely chemically exfoliated tens nm-thick $3R$-NbS_2 nanoplatelets[26] and low-pressure CVD synthetized eight-awn star $3R$-TaS_2.[27] However, the breakthrough performances of group-5 TMDs are typically reached after electrochemical preconditionings of the electrodes, namely thousands of cyclic voltammetry (CV) cycles or long-term (several hours) chrono/potentiometric tests.[20,21,26] Such in situ electrochemical treatments lead to a progressive fragmentation of the nanoplatelets, which evolve to even thinner morphologies.[20,21,26] The thick-to-thin morphology evolution of the nanoplatelets has a dual effect. Firstly, it facilitates the access of the aqueous protons (H_3O^+) to the catalyst films.[20,21,26] Secondly, it reduces the number of van der Waals gaps between the layers that the electrons need to overcome before reaching the electrode/electrolyte interface, in which the HER takes place.[20,21,26] However, an excessive fragmentation of the catalysts raises doubts concerning the possible and uncontrollable loss of catalytic materials or the delamination of the catalytic films from the electrode substrate. Therefore, the performance reliability of group-5 TMDs under high-rate H_2 production is still under debate.[28] Recently, $2H$-NbS_2 with an excess of Nb (i.e., $Nb_{1.35}S_2$) has been synthetized by CVD method to eliminate the van der Waals gap between the layers of the nanoplatelets, increasing the electrical conductivity of the nanoplatelets themselves (i.e., reducing the electron transfer resistance toward the surface, compared to the $2H$-NbS_2 reference) and conferring a structural stability.[28] Micro-electrochemical measurements have shown the possibility to attain a current density over 5 A cm^{-2} at an overpotential of ≈420 mV, leading to proof-of-concept electrolysers.[28] Nevertheless, the scalable production of this newly engineered compound and their integration in nanostructured electrodes, with industrial relevant mass loading, may be challenging for its use in real electrolysers. In our recent work, we have also shown that single-/few-layer $2H$-NbS_2 nanoflakes with an excess of Nb, produced by the scalable liquid-phase

exfoliation (LPE) method, can sustain high current densities (>100 mA cm^{-2}) at overpotentials even lower than those of commercial Pt on carbon (Pt/C), offering a pathway to use group-5 TMDs at industrial-scale.[29] Recently, we have achieved similar catalytic activities using LPE-produced H-TaS_2 nanoflakes in heterogeneous configurations with H-$TaSe_2$.[25] Lastly, theoretical calculations on group-5 TMDs have been theoretically proposed as ideal supports for anchoring single metallic atom catalysts (e.g., Pt, Pd, and Ni), boosting the utilization efficiency and the HER-activity of metals[30] and acting as scaffold for the realization of three-functional catalysts for the oxygen reduction and evolution reactions, and the HER. However, such effects have been rarely reported in experiments, and just treated as side-effects (i.e., electrolyte contaminations) to carefully discriminate for an accurate evaluation of the catalytic performance of the group-5 TMDs.[20,21,29] In order to provide further insights on the rational and practical use of 2D metallic group-S TMDs for the HER, we report the production and the engineering of a "newly discovered" phase of TaS_2, namely $6R$-TaS_2, through scalable LPE method, which is foreseen for industrial developments.[31] Noteworthy, the $6R$-TaS_2 is commonly mistaken with the 2H phase both at lab and commercial levels.[32] However, these two phases of TaS_2 significantly differ from each other. In fact, the 2H polytype is made of layers with trigonal prismatic Ta coordination (similarly to the $3R$-TaS_2),[33–35] while the $6R$ polytype alternates layers with trigonal prismatic and octahedral Ta coordination[36] (similarly to $4H_b$-TaS_2).[37] Therefore, these mixed coordinated polytypes can show properties resembling to those exhibited by either trigonal prismatic (2H or 3R) or octahedral (1T) phases,[38] stressing the need for multiple, careful material characterizations for the correct assignment of their phase. A novel liquid-phase microwave (MW) treatment is proposed to fragment the $6R$-TaS_2 nanoflakes, causing the evolution of extended, flat monocrystalline flakes into crinkled, partly polycrystalline ones. The optimization of the MW treatment lowers the η_{10} of our catalytic films from 0.377 to 0.192 V, suggesting the possibility to structurally engineer metallic TaS_2 nanoflakes, without recurring to any time-consuming in situ electrochemical methods.[20,21,26] Consequently, the MW-treated electrodes reach a MA of the $6R$-TaS_2 nanoflakes (MA_{TaS2}) of 100 A g^{-1} at an overpotential of 0.239 V. Lastly, we show a relationship between the structural properties of the nanoflakes and their activity to trap metal impurities, namely Pt species resulting by the dissolution of Pt counter electrodes during the long-term HER operation in acidic media. As supported by previous theoretical studies,[30] the MW-treated $6R$-TaS_2 nanoflakes enhance their HER-activity by trapping the dissolved Pt species. Consequently, the MA of Pt (MA_{Pt}) can reach values up to 10 000 A g$_{Pt}^{-1}$ at overpotential of only 50 mV, which is ≈20 times higher than the one measured for Pt nanoparticles in Pt/C (488 A g$_{Pt}^{-1}$ at the same overpotential of 50 mV). Our results clarify fundamental aspects of the catalytic phases of TaS_2, including surface oxidation effects, which are typically neglected in literature reporting record-high catalytic performance.[20] Moreover, we prove that the engineered $6R$-TaS_2 nanoflakes can be considered as efficient electrocatalysts for the HER, or used as ideal scaffolds to host noble metals with high MA for the HER, as well as for other electrochemical reactions.

**ADVANCED
SCIENCE NEWS**

www.advancedsciencenews.com

NANO · MICRO

small

www.small-journal.com

Figure 1. Structural, chemical, and morphological characterizations of the as-synthetized $6R$-TaS$_2$ crystals. a) XRD spectrum of the as-synthetized "$6R$-TaS$_2$" crystals. The reference pattern of $6R$-TaS$_2$ (ICSD-52117) and $2H$-TaS$_2$ (ICSD-68488) are also shown. The bottom row shows the magnifications of the XRD spectrum in relevant angle regions for the analysis. b) Crystal structure of the $6R$-TaS$_2$, consisting in a stack of layers alternating trigonal prismatic ($1H$) and octahedral ($1T$) Ta coordination. c) SEM image of the as-synthetized $6R$-TaS$_2$ crystals and d,e) the corresponding EDS maps for Ta (M line at 1.71 keV, in green) and S (Kα line at 2.31 keV, in violet).

2. Results and Discussion

2.1. Synthesis and Exfoliation of TaS$_2$ Crystals

The $6R$-TaS$_2$ crystals were synthesized by the direct reaction of the atomic elements, using Ta powder and S granules in quartz glass ampoule (see details in Supporting Information, Methods), following the protocols previously reported for the synthesis of $2H$-TaS$_2$.[39] We point out that when the material is prepared from Ta foil or wire, $2H$-TaS$_2$ is typically obtained.[33,36] Differently, when (partially oxidized) Ta powder is used as a starting material, $6R$-TaS$_2$ is synthesized instead of $2H$-TaS$_2$ (which, however, marginally contributed to the final crystal composition).[36] Generally, at the synthesis temperature used in our case, $2H$-TaS$_2$ is promoted in the presence of highly hydrogenated Ta, while a decrease of its hydrogenation level can result in the production of the $6R$ polytype (or even 1T polytype for dehydrogenated Ta).[40] Consequently, the release of oxygen from the Ta powder may decrease the hydrogen adsorbed on the Ta, promoting the formation of the $6R$-TaS$_2$. Since $6R$- and $2H$-TaS$_2$ show similar X-ray diffraction (XRD) patterns (see reference cards, i.e., ICSD-68488 for the $2H$-TaS$_2$ and ICSD-52117 for the $6R$-TaS$_2$), the $6R$ polytype has been easily mistaken for the $2H$ one. We verify this erroneous interpretation also on commercial product of $2H$-TaS$_2$,[32] for which

our XRD analysis clearly revealed that the $6R$-TaS$_2$ is the main phase of the product (Figure S1, Supporting Information). Similarly, $6R$-TaS$_2$ crystals were produced by our synthesis with a marginal contribution of the $2H$ phase, as shown by its XRD pattern in **Figure 1**a (no Ta$_2$O$_5$ was evidenced by XRD in the product). Figure 1b shows the crystal structure of the $6R$-TaS$_2$, consisting in a stack of layers alternating trigonal prismatic (1H) and octahedral ($1T$) Ta coordination.[33,34,36]

The as-produced $6R$-TaS$_2$ crystals were further characterized by scanning electron microscopy (SEM) coupled with energy-dispersive X-ray spectroscopy (EDS) (Figure 1c–e; Figure S2 and Table S1, Supporting Information), showing a S:Ta atomic ratio of 1.9 ± 0.2, which is in agreement with previous studies on TaS$_2$ using similar synthesis processes.[25,39,41] Noteworthy, the exceeding Ta may intercalate between the TaS$_2$ layers, partially eliminating van der Waals gaps, similarly to non-layered (3D) polytypes of group-5 TMDs (e.g., Nb$_{1+x}$S$_2$, x = 0.35).[28] Despite the excess of Ta, the SEM image of the as-synthetized crystals (**Figure 2**a) show layered edges, indicating a layered structure of our $6R$-TaS$_2$ crystals, which exhibit chalcogen vacancies. Thereafter, $6R$-TaS$_2$ crystals were successfully exfoliated via ultrasonication-assisted LPE[42] in anhydrous isopropyl alcohol (an-IPA) followed by a sedimentation-based separation[43] to remove the un-exfoliated material. In these steps, we have adapted protocols recently reported by our group for the group-5

ADVANCED
SCIENCE NEWS
www.advancedsciencenews.com

NANO · MICRO
small
www.small-journal.com
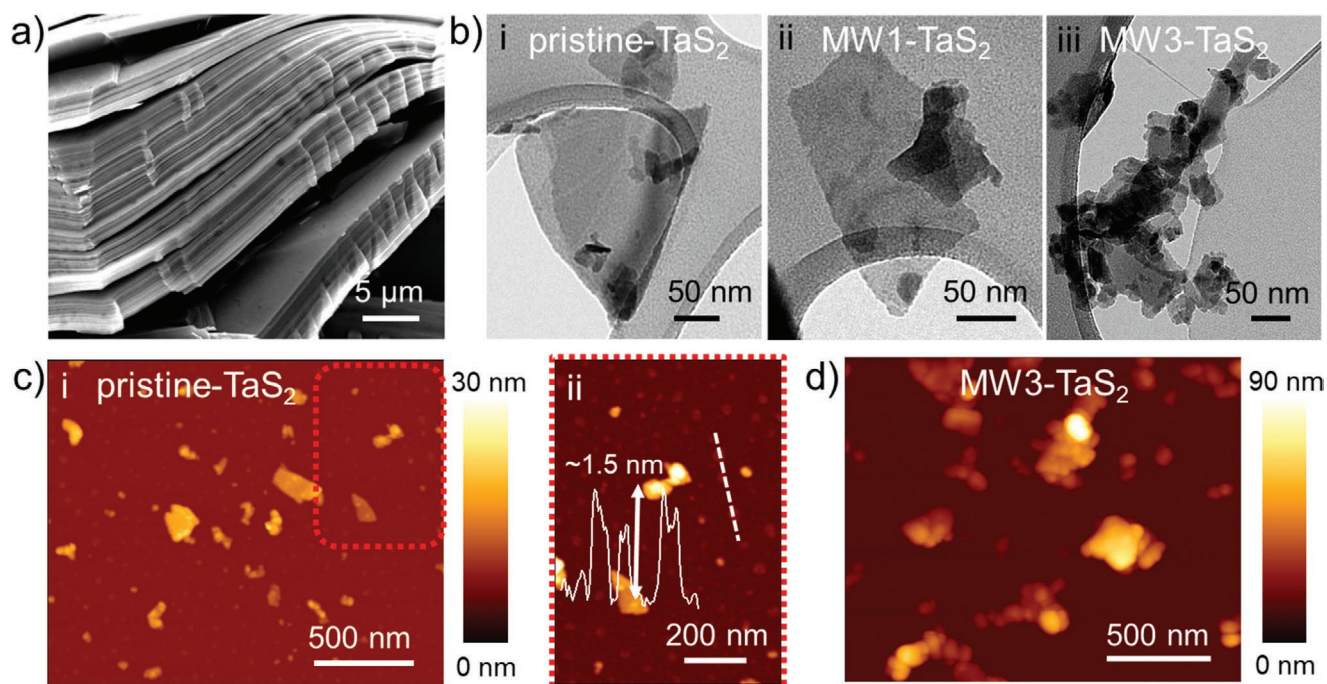
Figure 2. Morphology characterization of the LPE-produced *6R*-TaS$_2$ nanoflakes before and after the MW treatment. a) High-magnification SEM image of an edge of a *6R*-TaS$_2$ crystal, showing its layered structure. b) BFTEM images of representative nanoflakes in pristine-TaS$_2$ (panel i), MW1-TaS$_2$ (panel ii), and MW3-TaS$_2$ (panel iii). c) AFM image of nanoflakes in pristine-TaS$_2$ (panel i) and a zoom of a region showing single-/few-layer nanoflakes (panel ii). The height profile of single-/few-layer nanoflakes is also shown. d) AFM image of MW3-TaS$_2$, showing the presence of aggregates.

TMDs (see additional details in Supporting Information, Methods).[25,29] Afterward, the as-produced nanoflake dispersions were treated by MWs at 2.45 GHz in a home-like reactor operating at 560 W. Operatively, the proposed liquid-phase MW treatment shakes the nanoflake layers and the surrounding dispersing solvent, causing structural stresses on the material itself.[44] Actually, 2D TMDs are known to efficiently absorb MWs through: 1)"dipole polarization" of structural defects (e.g., elemental vacancies) and/or edges,[45,46] which behave as dipoles under an alternating electric field; 2) "interfacial polarizations" (or called Maxwell-Wagner-Sillars—MWS—polarizations)[47] at multiple interfaces among nanoflakes, which act as capacitor-like systems;[46,48] and 3) excitation of metallic phase electrons, which can move through electrically conductive networks via the inter-nanoflake electron hopping transport (modeled by resistance–inductance–capacitance coupled circuits).[45,46] Moreover, multiple scattering resulting by high surface nanoflakes can amplify the MW absorption of the nanoflakes.[46] Lastly, the dispersing solvent can also create MW-absorbing dipoles at the interfaces with the nanoflakes, or interact with MWs through the excitation of the dipole rotation. However, in our case, the dipole rotation of an-IPA is negligible due to its high rotational frequencies (>2.45 GHz).[49] The MW irradiation-induced modifications of the morphology of the nanoflakes are shown by bright-field TEM (BFTEM) (Figure 2b). The untreated sample (pristine-TaS$_2$) consists in nm-thick flakes, displaying wrinkled surfaces with irregular shapes, but sharp edges (Figure 2b, panel i). The data of the lateral size of the nanoflakes follow a log-normal distribution peaked at 24.6 nm (average values = 87.6 nm; maximum value = 751.1 nm) (Figure S3, Supporting Information).

After 1 min MW irradiation (sample named MW1-TaS$_2$), the nanoflakes retain their basal plane integrity, displaying lateral sizes slightly inferior to pristine-TaS$_2$ (average value = 64.1 nm; maximum value = 414.5 nm) (Figure S4, Supporting Information). However, their edges are jagged, indicating a perimeter modification. By further increasing the MW irradiation time up to 3 min (sample named MW3-TaS$_2$), the structure of the nanoflakes evolves toward minced irregular nanostructure having the tendency to aggregate. Atomic force microscopy (AFM) imaging shows that pristine-TaS$_2$ (Figure 2c) and MW1-TaS$_2$ (Figure S5, Supporting Information) mainly consist of single-layer/few-layer TaS$_2$ nanoflakes (being the AFM thickness of (*1H*) TaS$_2$ monolayer between 0.4 and 0.9 nm, depending on the TaS$_2$/substrate interaction).[50,51] Instead, nanostructure aggregates are mainly observed in MW3-TaS$_2$ (Figure 2d), in agreement with TEM analysis. Few aggregates are also observed in MW1-TaS$_2$, indicating a progressive evolution from the morphology of pristine-TaS$_2$ to MW3-TaS$_2$ with increasing the MW treatment duration. The thickness data of the nanoflakes follow a log-normal distribution for both pristine-TaS$_2$ (Figure S6, Supporting Information) and MW1-TaS$_2$ (Figure S7, Supporting Information), with peaks at 1.7 and 5.0 nm, respectively. The higher thickness of the nanoflakes in MW1-TaS$_2$ compared to pristine-TaS$_2$ is linked with their aggregation, which leads to an overestimation of the measured thickness values.

The crystallinity of the TaS$_2$ nanoflakes was confirmed by XRD measurements. As shown in Figure S8, Supporting Information, the XRD patterns of the exfoliated samples still show the main reflections of the as-synthetized *6R*-TaS$_2$ crystals. However, the broadening of their XRD peaks impedes

the reliable distinction of the *6R* and *2H* phases, which may coexist in the samples. Raman spectroscopy further confirms the crystallinity of the exfoliated samples (Figure S9, Supporting Information). Noteworthy, to the best of our knowledge, no studies reported the Raman characterization of the *6R*-TaS$_2$. Thus, our results, fully detailed in Supporting Information, provide novel spectroscopic information on such material polytype. X-ray photoelectron spectroscopy (XPS) measurements were performed to thoroughly analyse the chemical composition of the surface of the investigated materials. Although these are not studies focusing on the XPS characterization of the *6R*-TaS$_2$, it is known that the group-5 TMDs are susceptible to surface oxidation when exposed to ambient environments.[41,50] Therefore, care needs to be taken when these materials are used in practical applications (although recent works claimed the excellent electrochemical stability of the group-5 TMDs during their HER operation in acidic media[20,21,26]). In our case, the optimal fitting of the Ta 4f spectrum of the as-synthetized *6R*-TaS$_2$ crystals (**Figure 3**a) requires the use of four doublets. In the high binding energy side of the investigated range, the doublet with peaks at (26.5 ± 0.2) and (28.4 ± 0.2) eV is assigned to the Ta^{5+} state in Ta$_2$O$_5$, in agreement with previous literature.[52] In the low binding energy side, two doublets exhibit Ta 4f$_{7/2}$ peak positions at (23.1 ± 0.2) and (23.6 ± 0.2) eV, which are similar to those reported for the *1T* phase.[53] The presence of the two doublets in the *1T*-TaS$_2$ has been ascribed to the periodic atomic displacements of the room temperature nearly commensurate charge density wave phase.[34,54] Thus, our data suggest that the surface of the *6R*-TaS$_2$ crystals exhibits a CDW behavior similar to the *1T*-TaS$_2$. Lastly, the fourth doublet with the Ta 4f$_{7/2}$ peak

centered at (24.4 ± 0.2) eV is attributed to the presence of Ta sub-oxides.[55] The S 2p spectrum of the as-synthetized *6R*-TaS$_2$ crystals (Figure 3b) shows a doublet with the S 2p$_{3/2}$ component at (161.4 ± 0.2) eV, which is assigned to the sulphides.[52] More in detail, the peak positions of this S 2p doublet resemble those reported for the *1T*-TaS$_2$,[53,56] and thus support the assignment of the Ta 4f doublet peaks shown above. The XPS spectra of the exfoliated samples are reported in Figure 3c,d for pristine-TaS$_2$, and in Figure S10, Supporting Information for MW1-TaS$_2$ and MW3-TaS$_2$. Clearly, the samples exhibit similar features to each other, differing in part from what seen in the as-synthetized *6R*-TaS$_2$ crystals. In fact, additional Ta 4f and S 2p doublets with Ta 4f$_{7/2}$ peaks at (22.8 ± 0.2) and S 2p$_{3/2}$ peak at (160.9 ± 0.2) eV, respectively, are needed to achieve the best fit to the experimental data. Similar doublet peak positions have been reported for the *2H*-TaS$_2$.[21,53] Therefore, our XPS analysis suggests that the exfoliation of the *6R*-TaS$_2$ crystals may expose the *2H* phase as synthesis by-product buried deeper than the sensitivity depth of the technique in the bulk *6R*-TaS$_2$ crystals. Alternatively, the exfoliation of the *6R*-TaS$_2$ crystals into nanoflakes with less than 6 layers (i.e., the minimum number of layer compatible with the unit cell of the *6R* phase structure) can promote a phase conversion toward the *2H* phase. Beyond the emergence of the *2H* phase signatures, the intensities of the Ta$_2$O$_5$ doublet in the Ta 4f spectra increase in comparison to the as-synthetized crystals. In particular, Ta$_2$O$_5$ is now the most relevant Ta species, accounting for ≈50% of the total Ta content in pristine-TaS$_2$ and MW1-TaS$_2$. In the MW3-TaS$_2$, the Ta$_2$O$_5$ accounts ≈85–90% of the total Ta content, suggesting that it is mainly associated to the oxidation of the nanoflake edges. The increase
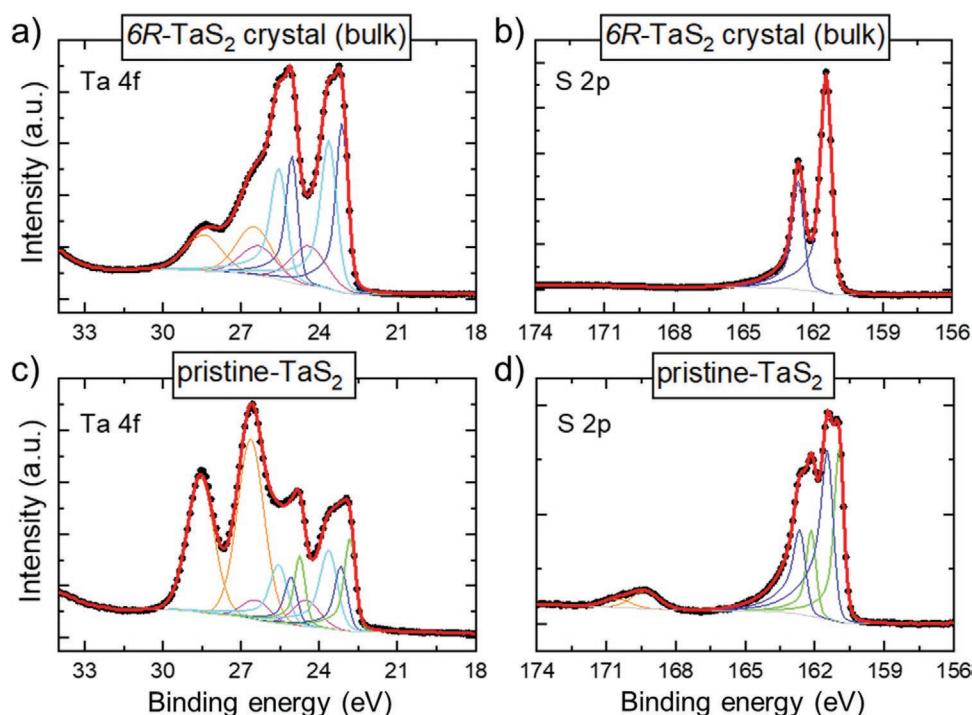

Figure 3. X-ray photoelectron spectroscopy characterization of the as-synthetized *6R*-TaS$_2$ crystals and the TaS$_2$ nanoflakes. a) Ta 4f and b) S 2p spectra of the *6R*-TaS$_2$ crystals (bulk sample). c) Ta 4f and d) S 2p spectra of the pristine-TaS$_2$ (exfoliated sample). The deconvolutions of the spectra are also shown to evidence the bands attributed to the different oxidation states of the elements.

of the oxidation level is further testified by the presence of a S 2p doublet with the S $2p_{3/2}$ peak at (169.4 ± 0.3) eV associated to the S^{6+} in SO_4^{2-}.[57] Although the surface oxidation of the group-5 TMDs is poorly discussed in HER-catalyst studies, it has also been evidenced by the previous XPS analyses.[21,39,41] Not rarely (and in relevant literature), the absence of TaS_2 oxidation has been claimed by erroneously attributing the Ta_2O_5 or Ta sub-oxide peaks to the TaS_2 (in such cases, the material surface was almost totally oxidized).[20]

High-resolution TEM (HRTEM) analyses were performed to examine in detail the evolution of the exfoliated samples with the MW treatments, in terms of crystallinity and morphology. **Figure 4**a shows an elastically filtered BFTEM image of representative nanoflakes in pristine-TaS_2. Figure 4b reports a HRTEM image of an extended, single-crystalline portion of the suspended region of the nanoflakes (panels i). The magnification of a portion of this HRTEM image (panel ii) and the fast Fourier transform (FFT) of the magnified region (panel

iii) show a single-crystalline structure, matching with the $2H$-TaS_2 one.[58] Given the low statistical significance of HRTEM analyses, the relatively large uncertainty in the measurement of the lattice spacings (up to 5%[59]) and angles in HRTEM, and the similarity between the $6R$- and $2H$-polytypes of TaS_2, a statistical information concerning the more abundant polytype cannot be based on HRTEM analyses. Contrary to pristine-TaS_2, only composed by single-crystal extended flakes, the HRTEM analysis of MW3-TaS_2 (Figure 4c,d) shows the presence of less extended, multiply folded polycrystalline flakes. Like MW3-TaS_2, structured TaS_2 flakes are also observed in MW1-TaS_2 (Figure S11, Supporting Information). Based on these results, Figure 4e shows a sketch of the morphological and structural evolution of the TaS_2 nanoflakes with increasing the duration of the MW treatments. An accurate explanation of the effects induced by MW treatment would need specific time-resolved atomic-scale imaging coupled with atomistic simulations, which is beyond the goals of this current work. However,
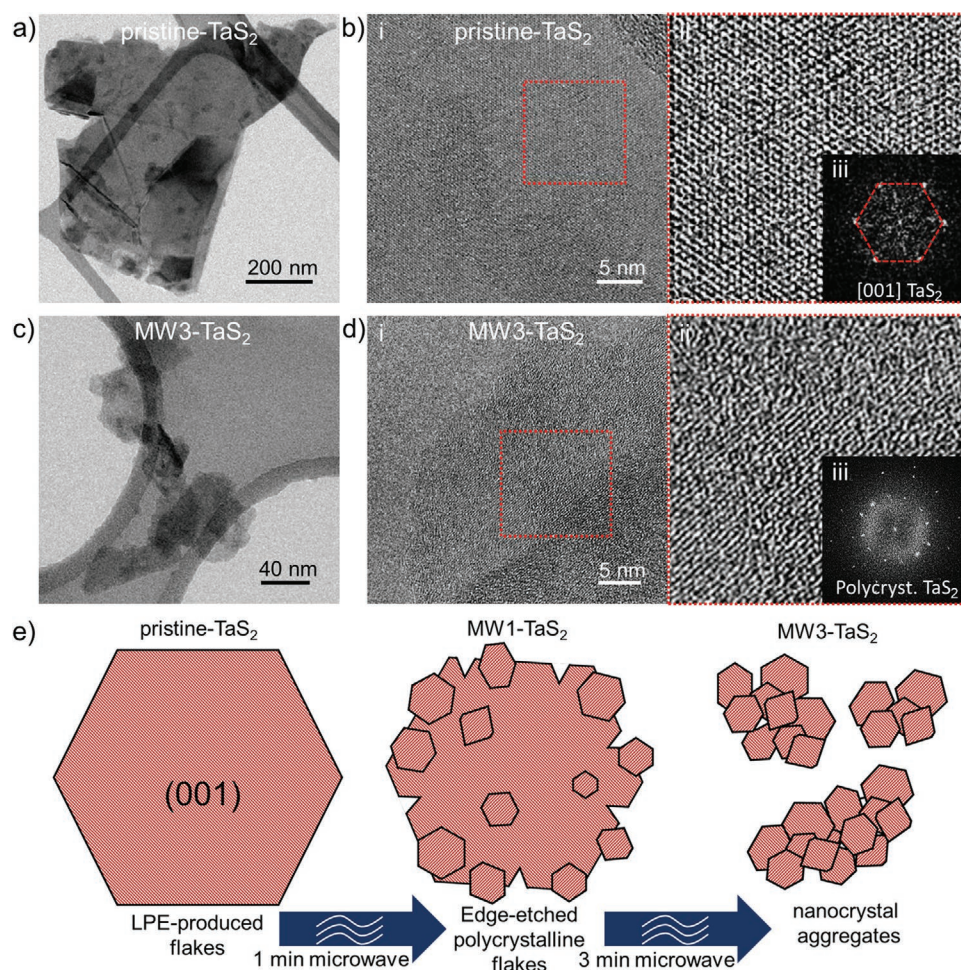

Figure 4. Morphology and structure evolution of the TaS_2 nanoflakes during the MW treatment. a) Elastically filtered BFTEM image of representative nanoflakes in pristine-TaS_2, partially suspended on a hole in the carbon support film. b) HRTEM image of a portion of the suspended region of a nanoflake (panel i), its magnified region (panel ii) and the FFT of the area delineated in the magnified image, matching the one of [001]-oriented $2H$-TaS_2 (panel iii). c) Elastically filtered BFTEM image of representative nanoflakes in MW3-TaS_2, some of them partially suspended on the holes in the carbon support film. d) HRTEM image of a portion of the suspended region of a nanoflake (panel i), its magnified region (panel ii), and the FFT of the area delineated in the magnified image, matching the polycrystalline $2H$-TaS_2 (panel iii). e) Sketch of the morphological and structural evolution of the TaS_2 nanoflakes with increasing the MW irradiation time.

**ADVANCED
SCIENCE NEWS**

www.advancedsciencenews.com

NANO · MICRO

small

www.small-journal.com

we speculate that MWs, once absorbed by TaS_2 nanoflakes and converted to thermal energy, can provide sufficient energy to overcome the energy barrier for the migration of chalcogen-vacancies, interstitial atoms, and adatoms, as shown for other TMDs (e.g., MoS_2[60–62] WS_2,[63] and $MoSe_2$[64]). The coalescence of dislocations, as those intrinsically present at the edges, could form dynamic grain boundaries[60,63] and line defects.[61,62] Then, the sliding of grain boundaries can fragment the starting nanoflakes, while the strain fields of intersected networks of long line defects can trigger large-scale atomic reconstruction (i.e., inversion domains).[61,64] Overall, these effects can originate the monocrystalline-to-polycrystalline structure conversion in our TaS_2 nanoflakes during the MW irradiation.

2.2. Fabrication and Characterization of TaS_2-Based Electrodes

The electrodes were fabricated by depositing the TaS_2 nanoflake dispersions (catalyst mass loading = 0.2 mg cm^{-2}) onto carbon nanotube (CNT)-based papers (i.e., buckypapers) through vacuum filtration method (see details in Supporting Information, Methods). The choice of buckypaper as the support relies on data from our previous works, in which we showed that the porosity of the CNT tangle promotes the adhesion of the TMDC films without the need of any ion conducting binders,[65,66] such as sulfonated tetrafluoroethylene-based fluoropolymer copolymers (e.g., Nafion). The surface morphology of the as-prepared electrodes was characterized by SEM imaging (Figure S12, Supporting Information). In all the electrodes (hereafter named with the name of the corresponding catalysts, that is, pristine-TaS_2, MW1-TaS_2 and MW3-TaS_2), the TaS_2 nanoflakes uniformly cover the CNT tangle. **Figure 5**a shows the linear sweep voltammetry (LSV) scans in 0.5 M H_2SO_4 for the investigated electrodes. The data show that the MW treatments increase the HER-activity of pristine-TaS_2.

In particular, η_{10} decreases from 0.377 V for pristine-TaS_2 to 0.192 V for MW1-TaS_2. By further increasing the duration of the MW treatments to 3 min, the resulting electrode (MW3-TaS_2) shows a decrease of the HER-activity (η_{10} = 0.339 V) compared to MW1-TaS_2. This indicates that an excessive fragmentation of the basal plane of the nanoflakes is not beneficial for the performance of our catalysts. Both the LSV curves of the electrodes based on MW-treated TaS_2 nanoflakes show cathodic current densities starting at positive potential versus RHE and peaked at ≈−0.035 V versus RHE (Figure S13, Supporting Information). Such current densities cannot be attributed to the HER and might be correlated with a reduction of MW-treated TaS_2 nanoflakes, whose reactive edges may lead to a rapid reversible surface oxidation. Alternatively, structural modifications caused by the release of sulphur in the form of gaseous H_2S, as shown for MoS_x catalysts,[67] may cause of this cathodic current densities. Currently, a clear identification of the origin of these reduction peaks is still needed. To improve further the HER-activity of the MW-treated TaS_2 nanoflakes, pristine-TaS_2 and MW1-TaS_2 were electrochemically treated by subsequent CV scans (4000 cycles), using both graphite rod (electrodes named pristine-TaS_2-CV_G and MW1-TaS_2-CV_G) and Pt wire (electrodes named pristine-TaS_2-CV_{Pt} and MW1-TaS_2-CV_{Pt}) as the counter electrodes. In fact, as the HER proceeds, it has been reported that the group-5 TMDs exhibit an unusual ability to self-optimize their morphology for an optimal charge transfer and an elevate accessibility of their active sites.[20,21,26] Figure 5b shows the LSV curves of the investigated electrodes, evidencing that CV cycling enhances the HER-activity of the designed electrodes. The self-optimizing behavior using graphite rod as counter electrodes confirms the results previously reported in literature,[20,21,26] for which the Pt contamination of the working electrodes was carefully excluded. Therefore, the electrochemical treatment further lowered the η_{10} of the as-produced electrode to 0.241 V for pristine-TaS_2-CV_G and 0.119 V for MW1-TaS_2-CV_G.
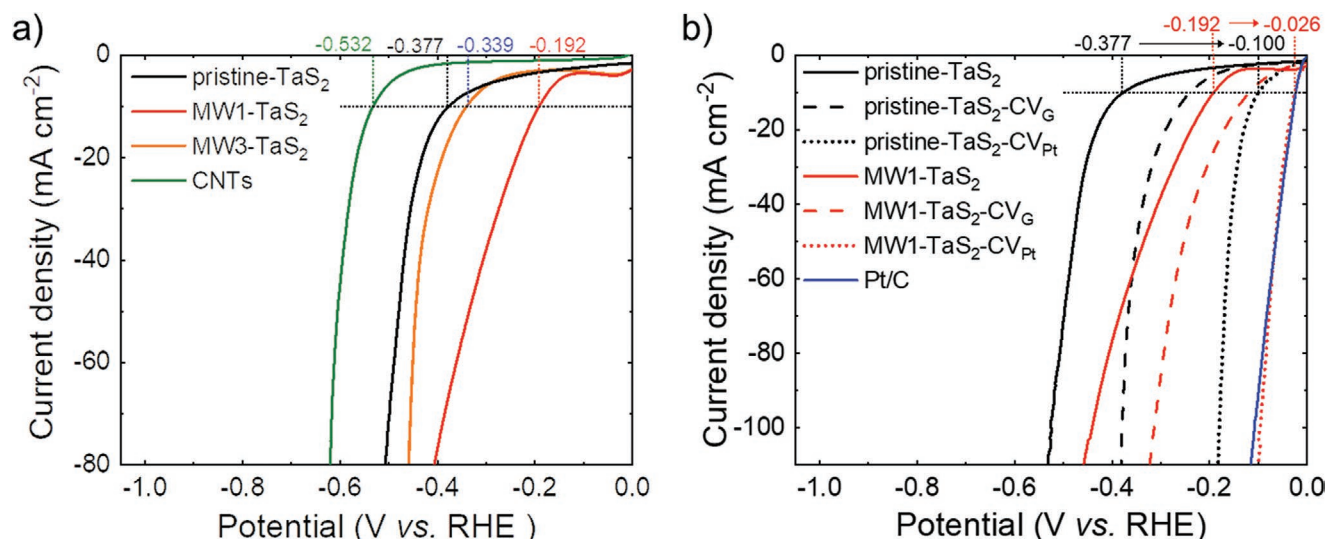
Figure 5. Electrochemical characterization of the TaS_2-based electrodes. a) LSV curves measured for pristine-TaS_2, MW1-TaS_2, and MW3-TaS_2 in 0.5 M H_2SO_4. b) LSV curves measured for the as-produced electrodes (pristine-TaS_2 and MW-TaS_2) and the electrochemically treated electrodes with graphite rod (pristine-TaS_2-CV_G and MW1-TaS_2-CV_G) or Pt wire (pristine-TaS_2-CV_{Pt} and MW1-TaS_2-CV_{Pt}) as the counter electrodes. The LSV curves measured for the CNTs (electrode substrate) are also shown. The η_{10} values measured for each electrode are indicated.

Noteworthy, when the Pt wire was used as the counter electrode, the strong improvement of the HER-activity of the electrodes suggest that the electrodes efficiently uptake the Pt species that are dissolved by the counter electrode. More in detail, this process is particularly effective for the MW-treated catalysts. In fact, MW1-TaS$_2$-CV$_{Pt}$ exhibits an HER-activity almost identical to the one of our Pt/C reference (η_{10} = 0.026 V). These observations support the presence of a relationship between the Pt electrochemical deposition on TaS$_2$ nanoflakes and the structural properties of the latter, and the MW treatment can be used to control the Pt uptake for the fabrication of highly HER-active electrodes. The presence of Pt on our electrodes after CV cycling was confirmed by SEM-coupled EDS and XPS measurements (Figures S14 and S15, Supporting Information, respectively). Raman spectroscopy and HRTEM analyses (Figures S16 and S17, Supporting Information, respectively) support that the TaS$_2$ nanoflakes preserve their native structure, in agreement with previous works. However, XPS measurements revealed an increase of surface oxides (i.e., Ta$_2$O$_5$ and sulphates) (Figure S18, Supporting Information). These results contrast with previous studies, which claimed a perfect (electro)chemical stability of the TaS$_2$[20,21] and similar group-5 TMD catalysts,[26] during the HER-operation. However, to support this crucial claim, no thorough XPS analyses were performed after electrochemical tests, or an erroneous attribution of the XPS peak was presented (in such cases, the surface of the materials was oxidized).[20] To now, we have two possible explanations for the oxidation of the surface of the TaS$_2$ nanoflakes. The first one is linked with the oxidation of the TaS$_2$ nanoflakes that occurs during the drying of the electrode following the electrochemical test prior to the acquisition of their XPS spectra. The second one, instead, could be related to the oxidation of the TaS$_2$ nanoflakes occurring while they catalyze the HER process. In this latter case, the formed oxides atop the TaS$_2$ nanoflakes are not catalytically active for the HER but can interact with the TaS$_2$ nanoflakes to regulate the HER-activity of the electrodes.
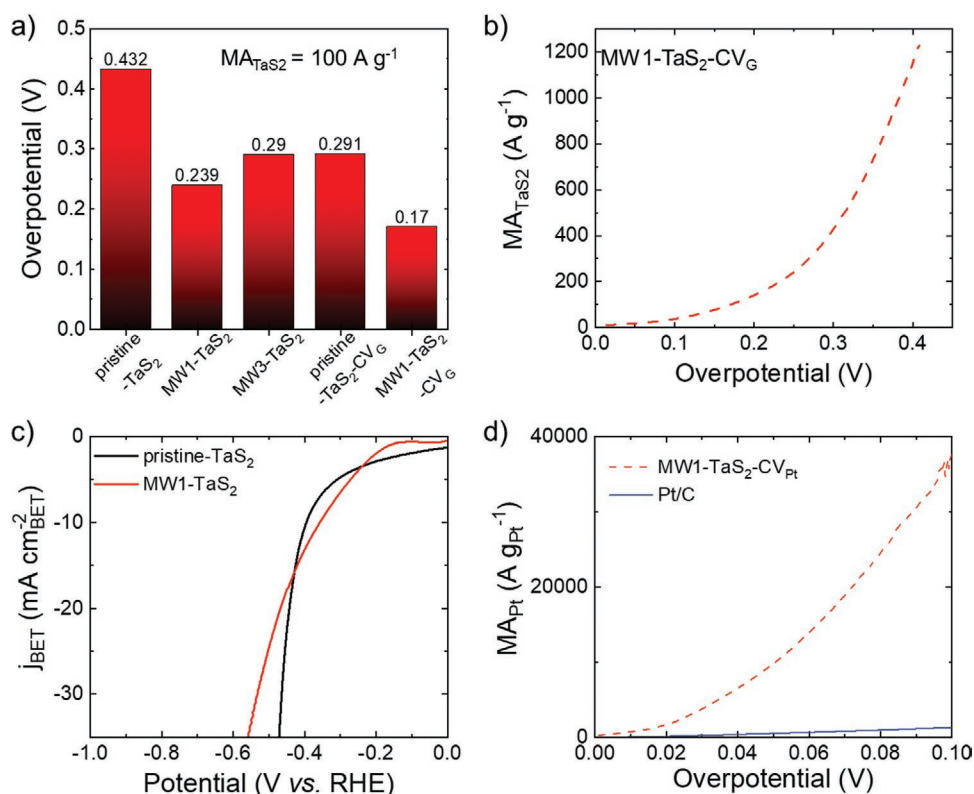
2.3. Analysis of the Intrinsic Catalytic Activity of the TaS$_2$ Nanoflakes

In order to evaluate the intrinsic HER-activity of a catalyst, it is common practice to analyse both the MA, that is, the mass loading normalized-activity (MA), and the specific activities (or real surface area-normalized activities), that is, the electrochemically accessible/active surface area (ECSA)-normalized activity (j_{ECSA}) or the Brunauer–Emmett–Teller (BET) surface area-normalized activity (j_{BET}).[68,69] In this work, we avoid the evaluation of j_{ECSA}, since the presence of highly porous supports (such as buckypapers) leads to a significant overestimation of the ECSA of the catalytic films when traditional ECSA measurement methods are used (e.g., double-layer capacitance—C$_d$—measurement by means of CV measurements at different scan rates in a non-faradaic region).[70] In fact, the overestimation of the ECSA can result in a severe underestimation of the specific activity. Consequently, our analysis mainly focused on the MA and the j_{BET} as relevant activity metrics. By weighting the electrodes before and after the deposition of the catalytic films, the mass loading of the TaS$_2$ nanoflakes for the as-produced electrodes

was measured to be ≈0.20 mg cm^{-2}. The Pt uptake after the electrochemical tests using the Pt wire as the counter electrode was estimated through inductively coupled plasma-optical emission spectrometry (ICP-OES), digesting the samples in HCl (35%):HNO$_3$ (65%) (3:1 v/v) and 1:100 diluted HF (40–45%) for the Pt and the Ta detection, respectively. The S content after the electrochemical tests was not evaluated due to possible overestimation originated by residuals of the acidic electrolyte (i.e., 0.5 M H$_2$SO$_4$). Thus, we assumed an S:Ta atomic ratio of 1.9, as measured for the as-synthesized crystals, to measure the Pt weight content relatively to both S and Ta. Since possible S losses occurring during electrochemical tests were neglected, the real MA might have been underestimated in this work. This means that the conclusions that we will show hereafter are likely even more promising in terms of MA performance for prospective catalyst engineering activities. The estimated Pt mass loading (i.e., uptake) after 4000 CV cycles is 2.7 µg cm^{-2} for MW1-TaS$_2$-CV$_{Pt}$. For pristine-TaS$_2$-CV$_{Pt}$, the amount of Pt is below the detection limit of our ICP-OES setup. However, ICP-mass spectroscopy estimated a Pt mass loading of ≈0.1 µg cm^2, which is ≈27 times lower than the one measured for MW1-TaS$_2$-CV$_{Pt}$. These results indicate that the MW treatments enhance the capability of the TaS$_2$ nanoflakes to trap the Pt species during the CV experiments, as supported by the electrochemical characterizations above discussed (see LSV analysis, Figure 5b). The BET analysis was carried out on the exfoliated samples, (dried under inert atmosphere in form of powder) before and after the MW treatment, through physisorption measurements using Kr at 77 K as the gas carrier. Noteworthy, Kr was preferred to N$_2$ because the quadrupole moment of N$_2$ (0.27 Å^2)[71] limits the access of the gas into micropores, while Kr does not have a quadrupole moment and can easily access the micropores up to its cross-sectional area (between 0.11 and 0.22 nm^2 per atom at 77 K, depending on possible arrangements of adsorbed species on surface, as well as appropriate ranges of relative pressure used for BET measurements).[72] In addition, the low vapor pressure of Kr at 77 K enables a precise determination of the number of adsorbed molecules in presence of microporous materials with small surface areas and samples of low weight (e.g., thin films), in which the adsorption is typically performed in the 05 to 0.3 p/p0 BET-range at 77 K. Figure S19, Supporting Information shows the isotherms and the corresponding BET-isotherms obtained from the Kr physisorption measurements at 77 K on pristine-TaS$_2$ and MW1-TaS$_2$. The calculated BET specific surface areas (SSA_{BET}) of the catalysts are 6.0 m^2 g^{-1} for pristine-TaS$_2$ and 29.2 m^2 g^{-1} for MW1-TaS$_2$. Thus, apart influencing the Pt trapping, the MW treatment improve the surface area of the electrodes because of the nanoflake fragmentation, as also proved by the TEM analysis (see Figure 4). The concomitant increase of both Pt uptaking and surface area suggests an active role of the "defective" edges of TaS$_2$ in trapping Pt species, as recently observed for the case of other TMDs, for example, 2H-WS$_2$.[73]

Figure 6a shows the overpotential of pristine-TaS$_2$, MW1-TaS$_2$, and MW3-TaS$_2$ corresponding to a MA of TaS$_2$ (MA$_{TaS2}$) of 100 A g^{-1}. The most performant electrode (MW1-TaS$_2$) exhibits an overpotential of 0.239 V. After 4000 CV cycles using graphite rod as the counter electrode (electrode named MW1-TaS$_2$-CV$_G$), the overpotential decreased to 0.170 V, which is inferior to the values reported in literature for many group-5 TMDs (see Table S2,

ADVANCED
SCIENCE NEWS
www.advancedsciencenews.com

NANO · MICRO
small
www.small-journal.com

Figure 6. Analysis of the intrinsic catalytic activity of the TaS_2 nanoflakes and TaS_2-trapped Pt. a) Overpotential at MA_{TaS2} of 100 A g^{-1} measured for the investigated electrode using the graphite rod as the counter electrode. b) MA_{TaS2} versus overpotential curve of MW1-TaS_2-CV_G. c) J_{BET} versus potential curves of pristine-TaS_2 and MW1-TaS_2. d) MA_{Pt} versus potential curves of MW1-TaS_2-CV_{Pt} and Pt/C.

Supporting Information). Figure 6b displays the MA_{TaS2} versus overpotential plot for MW1-TaS_2-CV_G, indicating the possibility to reach a MA_{TaS2} above 1000 A g^{-1} at overpotential higher than 0.38 V. Figure 6c shows the J_{BET} versus potential curves measured for pristine-TaS_2 and MW1-TaS_2 (Figure 1d). In such curves, the difference in the specific activity values between the two electrodes are significantly reduced compared to the MA_{TaS2}. Thus, these results support the fact that the MW-induced fragmentation of the TaS_2 nanoflakes causes an increase of the exposed catalytic surface area of their films, thus increasing the MA_{TaS2}. Therefore, the effect of the MW treatment resembles the fragmentation of the catalyst occurring during CV cycling, which is, however, highly time-consuming and raises doubts concerning the progressive dissolution of the catalytic materials when high-mass loading electrodes are used for high-rate H_2 production.[28] The downshift of the HER-overpotential of MW1-TaS_2 compared to pristine-TaS_2 may be ascribed to the activity of the nanoflakes edges in catalyzing the HER. However, at high current densities (>20 mA cm^{-2}), the HER-activity of the electrodes is still likely dominated by the basal planes of the nanoflakes, in agreement with previous theoretical and experimental studies on the group-5 TMDs.[20,21,74,26]

In addition to the MA_{TaS2}, the MAs of Pt (MA_{PtS}) for the electrodes after 4000 CV cycles using the Pt wire as the counter electrode (i.e., pristine-TaS_2-CV_{Pt} and MW1-TaS_2-CV_{Pt}) were also analyzed together with the one measured for the Pt/C reference. Noteworthy, the MA_{Pt} was estimated by subtracting the MA_{TaS2} of the electrode cycled with the graphite rod as the counter

electrode (i.e., MW1-TaS_2-CV_G) from the overall MA activity of the electrode cycled with the Pt wire as the counter electrodes (i.e., MW1-TaS_2-CV_{Pt}). Figure 6d shows the MA_{Pt} measured for the MW1-TaS_2-CV_{Pt} and the Pt/C. The data reveal that the Pt trapped by TaS_2 nanoflakes is extremely HER-active in comparison with the Pt nanoparticles in commercial Pt/C. In particular, MW1-TaS_2-CV_{Pt} shows a MA_{Pt} of 10 000 and 20 000 A g_{Pt}^{-1} at overpotentials as low as 50 and 72 mV, respectively.

Figure 7 reports the comparison of MA_{Pt} measured for various single atoms or Pt-based HER catalysts reported in literature. These values are significantly superior to those recently reported for Pt trapped by 2D MXene, namely $Mo_2TiC_2T_x$ (MA_{Pt} = 8300 A g_{Pt}^{-1} at overpotential = 77 mV),[75] and similar to the one recently reported by our group on more complex systems, namely octapod-shaped CdSe nanocrystals ($MA_{Pt} \approx 20\,000$ A g_{Pt}^{-1} at overpotential = 50 mV).[76] They are also comparable to the ones achieved by more complex atomic layer-deposition-based synthesis of N-doped graphene-supported single atom/cluster Pt (MA_{Pt} = 10 100 A g_{Pt}^{-1} at overpotential = 50 mV).[77] Overall, our data support that the interaction between Pt and TaS_2 nanoflakes is effective to maximize the MA_{Pt} toward record-high values, as discussed in the next section.

2.4. Theoretical Commentary on the HER-Activity of Group-5 TMDs and Trapped Metals

The HER-activity of group-5 TMDs has been discussed in recent works, and it is out of scope to reproduce their
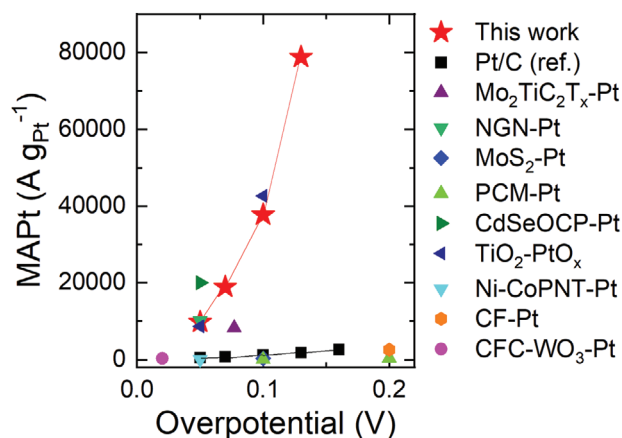
Figure 7. Catalytic performance of Pt in our electrodes based on TaS_2 nanoflakes and other single atom and cluster Pt-based catalysts. Comparison between the MA_{Pt} of our MW1-TaS_2-CV_{Pt} and other Pt-based catalyst reported in literature. The following nomenclature is used in the figure to refer to catalyst: $Mo_2TiC_2T_x$-Pt for single atom Pt immobilized on MXene nanosheets,[75] NGN-Pt for N-doped graphene nanosheets supported single atom and cluster Pt,[77] MoS_2-Pt for Pt atom-doped, few-layer MoS_2 nanosheets,[78] PCM-Pt for Pt atoms in the nitrogen-containing porous carbon matrix,[79] CdSeOCP-Pt for Pt immobilized on octapod-shaped CdSe,[76] TiO_2-Pt for sub-nanometric PtO_x clusters uniformly dispersed on a TiO_2 support,[80] Ni-CoPNT-Pt single Pt atoms on CoP-based nanotube arrays supported by a Ni foam,[81] CF-Pt for Pt nanoparticles on carbon foam,[82] and CFC-WO_3-Pt for atom cluster Pt dispersed in carbon fiber cloth supported WO_3.[83]

theoretical outcomes. Here, we just stress that, contrary to group-6 TMDs, metallic group-5 TMDs (e.g., TaS_2 and NbS_2) theoretically display HER-active basal planes beyond catalytic edge sites.[20–24,26] Consequently, the overall number of the catalytic sites expressed by both edges and basal plane can be significantly increased by order of magnitude compared to the other type of TMDs, including the widely investigated group-6 TMDs in their semiconducting phase (e.g., $2H$-MoS_2), whose HER-activity is based on their edges.[15–17,23] In our experiments, we show that a liquid-phase MW treatment in a home-like reactor can be used as alternative to electrochemical ones (i.e., thousands of CV cycles)[20,21,26] to increase the specific surface area of the TaS_2 nanoflakes produced by scalable LPE of native crystals. In particular, similarly to the treatment of the electrodes with thousands of CV cycles, the proposed MW treatment causes a fragmentation of the TaS_2 nanoflakes, which consequently improve their catalytic performance when incorporated in electrodes, as discussed in literature.[20,21,26]

However, supplementary considerations are needed to unravel the additional effects, beyond the initial HER-activity, observed for the TaS_2 nanoflakes after thousands of CV cycles using Pt wire as the counter electrode. The effects are summarized as the following: 1) the capability of the TaS_2 nanoflakes to efficiently uptake metal species (in particular Pt); 2) the high MA_{Pt} of the Pt electrodeposited onto TaS_2 nanoflakes. Although several 2D materials, including graphene,[77] MXenes,[75] and group-6 TMDs (e.g., MoS_2[84] and WS_2[73]) have been reported to efficiently trap highly HER-active metal impurities during both synthesis and electrochemical testing, we noticed that these effects are especially relevant for TaS_2 nanoflakes. In particular,

in our previous work on group-5 TMDs,[25,29] we immediately observed Pt contamination on the electrodes when Pt counter electrode were used. In particular, the metal impurities strongly affected the recorded HER-activity over ten minutes. Based on our experience, the effects of Pt impurities on the HER-activity were significantly more pronounced compared to the case of other group-6 TMDs, forcing the use of graphite rod as the counter electrode as a best practice to avoid wrong interpretation of electrochemical data. In addition, the electrolytic solution was refreshed before each experiment, and possible metal impurities of the starting electrolyte reagent were analyzed to exclude other metallic impurities in the starting electrolyte medium. Meanwhile, a theoretical work screened 48 combinations of metal atoms anchored on (defective) group-5 and group-6 (2D) TMDs.[30] The DFT calculations revealed that group-10 metal atoms (i.e., Ni, Pd, and Pt) strongly adsorb on S-deficient TMDs, much more than group-11 metals (i.e., Cu, Ag, and Au). In particular, the binding energy (E_b) of Pt anchored on TMDs is more negative than −6 eV.[30] The strongest binding occurs between Pt atoms and Ta-based TMDs, showing E_b of the anchored Pt significantly more negative than the experimental cohesive energy (E_{coh}) of atomic Pt ($\approx$−5.8 eV),[85] that is, the energy required to disintegrate Pt crystal into single atoms.[86] **Figure 8**a reproduces the results obtained for the specific case of 1H-TaS_2.[30]

These data show that the Pt atoms can be favorably and stably immobilized on our TaS_2 nanoflakes, especially in presence of abundant defects, as those originated by both MW and electrochemical treatments. In addition to the tendency of 2D supports to trap metal atoms, the free energy for hydrogen adsorption (ΔG_{Hads}) on such trapped Pt atoms is also a primary factor determining their catalytic activity.[87] In fact, in acidic media, the HER proceeds through an initial discharge of the hydronium ion (H_3O^+) and the formation of atomic H adsorbed on the electrocatalyst surface (H_{ads}) (H_3O^+ + e^- $\rightleftarrows$ H_{ads} + H_2O), followed by either an electrochemical Heyrovsky step (H_{ads} + H_3O^+ + e^- $\rightleftarrows$ H_2 + H_2O) or a chemical Tafel recombination step ($2H_{ads}$ $\rightleftarrows$ H_2).[88] The optimal balance between adsorption and desorption steps leads to an efficient HER, as described by the empirical Sabatier principle exemplified by the so-called Volcano plot.[87] In brief, a candidate HER-catalyst must show a ΔG_{Hads} close to 0 eV. The ΔG_{Hads} for Pt atoms adsorbed onto the 1H-TaS_2 layer has been predicted to be close to zero ($\approx$0.1 eV) (Figure 8b).[30] The catalytic activity of Pt atoms trapped by TaS_2, as well as the high utilization efficiency in presence of isolated Pt atoms, theoretically support the ultrahigh MA_{Pt} observed for our MW1-TaS_2-CV_{Pt}.

3. Conclusion

In summary, a liquid-phase MW treatment in a home-like reactor has been proposed to control the structural and morphological properties of model-type solution-processed 2D metallic TMDs, namely TaS_2 nanoflakes, produced by ultrasonication-assisted LPE method of "newly discovered" 6R-TaS_2 crystals. In particular, the proposed MW treatment fragments the metallic nanoflakes, which consequently evolve from a monocrystalline to a polycrystalline structure. The modification of the structural properties regulates the HER-activity of the TaS_2 nanoflakes, lowering
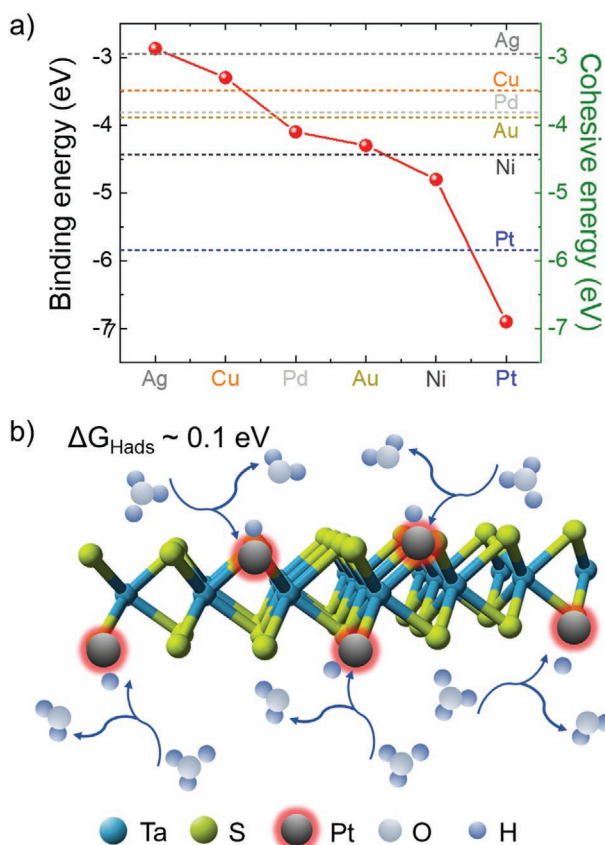
Figure 8. Trapping of Pt atoms by TaS_2 nanoflakes and resulting HER-activity. a) Binding energy between metal atoms and $1H$-TaS_2 and cohesive energy for each metal. b) Sketch of a $1H$-TaS_2 layer trapping a Pt atom in a S-deficient defect. The hybrid system catalyzes the Vomer step of the HER on Pt centers while maximizes the utilization efficiency of Pt. The data values have been taken from ref. [30]

be engineered by means of viable processes to act as efficient HER-catalysts and ideal noble metal-immobilizing 2D scaffolds with extreme HER-activities. In addition, our material data warn researchers on misleading data interpretation during the characterization of the TaS_2- and other group-5 TMDs, since an ultralow level of metal impurities could drastically enhance their catalytic performance. Lastly, our spectroscopic and microscopic analyses aim to elucidate essential and unclarified aspects regarding the phase and surface chemistry of TaS_2 materials reported in the field of electrocatalysis.

Supporting Information

Supporting Information is available from the Wiley Online Library or from the author.

Acknowledgements

Conflict of Interest

The authors declare no conflict of interest.

Keywords

the overpotential at a cathodic current of 10 mA cm^{-2} (η_{10}) from 0.377 to 0.192 V. The optimized electrodes reach a MA of the TaS_2 nanoflakes (MA_{TaS2}) of 100 A g^{-1} at an overpotential of 0.239 V, and above 1000 A g^{-1} at overpotentials higher than 0.38 V. The effect of our MW treatment resembles the self-optimizing fragmentation of the 2D group-5 TMDs occurring during in situ electrochemical preconditioning of the electrodes. Such self-optimizing fragmentation has been further utilized to reduce the η_{10} of our optimized electrodes to 0.119 V (after 4000 cyclic voltammetry—CV—cycles). Additionally, MW-treated TaS_2 nanoflakes are proved to be extremely effective in trapping Pt contaminations, which originate by the dissolution of Pt counter electrode in acidic media during long-term electrochemical tests. Consequently, the Pt-trapped electrodes display outstanding HER-activities, corresponding to MA of Pt (MA_{Pt}) of 10 000 and 20 000 A g$_{Pt}^{-1}$ at overpotentials as low as 50 and 72 mV, respectively. These MA_{Pt} values are ten times superior to the ones measured for Pt/C reference, probably representing state-of-the-art values. In-depth analysis of theoretical works supports the occurrence of a strong and stable anchoring of Pt atoms on defective $1H$-TaS_2. Such Pt/$1H$-TaS_2 interaction can maximize the utilization efficiency of the Pt, while retaining its catalytic efficiency. Our results indicate that TaS_2 nanoflakes can

[1] D. P. Gregory, *Sci. Am.* **1973**, *228*, 13.
[2] M. Ball, M. Weeda, *Int. J. Hydrogen Energy* **2015**, *40*, 7903.
[3] O. Schmidt, A. Gambhir, I. Staffell, A. Hawkes, J. Nelson, S. Few, *Int. J. Hydrogen Energy* **2017**, *42*, 30470.
[4] M. Schalenbach, G. Tjarks, M. Carmo, W. Lueke, M. Mueller, D. Stolten, *J. Electrochem. Soc.* **2016**, *163*, F3197.
[5] K. Zeng, D. Zhang, *Prog. Energy Combust. Sci.* **2010**, *36*, 307.
[6] K. C. Neyerlin, W. Gu, J. Jorne, H. A. Gasteiger, *J. Electrochem. Soc.* **2007**, *154*, B631.
[7] J. Durst, C. Simon, F. Hasche, H. A. Gasteiger, *J. Electrochem. Soc.* **2015**, *162*, F190.
[8] T. Reier, M. Oezaslan, P. Strasser, *ACS Catal.* **2012**, *2*,1765.
[9] S. Cherevko, S. Geiger, O. Kasian, N. Kulyk, J.-P. Grote, A. Savan, B. R. Shrestha, S. Merzlikin, B. Breitbach, A. Ludwig, K. J. J. Mayrhofer, *Catal. Today* **2016**, *262*, 170.

ADVANCED
SCIENCE NEWS
www.advancedsciencenews.com

NANO · MICRO
small
www.small-journal.com

[10] C. Sealy, *Mater. Today* **2008**, *11*, 65.

[11] C. G. Morales-Guio, L.-A. Stern, X. Hu, *Chem. Soc. Rev.* **2014**, *43*, 6555.

[12] X. Zou, Y. Zhang, *Chem. Soc. Rev.* **2015**, *44*, 5148.

[13] J. Kibsgaard, I. Chorkendorff, *Nat. Energy* **2019**, *4*, 430.

[14] Q. Lu, Y. Yu, Q. Ma, B. Chen, H. Zhang, *Adv. Mater.* **2016**, *28*, 1917.

[15] T. F. Jaramillo, K. P. Jørgensen, J. Bonde, J. H. Nielsen, S. Horch, I. Chorkendorff, *Science* **2007**, *317*, 100.

[16] D. Voiry, M. Salehi, R. Silva, T. Fujita, M. Chen, T. Asefa, V. B. Shenoy, G. Eda, M. Chhowalla, *Nano Lett.* **2013**, *13*, 6222.

[17] J. Kibsgaard, Z. Chen, B. N. Reinecke, T. F. Jaramillo, *Nat. Mater.* **2012**, *11*, 963.

[18] H. Li, C. Tsai, A. L. Koh, L. Cai, A. W. Contryman, A. H. Fragapane, J. Zhao, H. S. Han, H. C. Manoharan, F. Abild-Pedersen, J. K. Nørskov, X. Zheng, *Nat. Mater.* **2016**, *15*, 48.

[19] C. Tsai, K. Chan, F. Abild-Pedersen, J. K. Nørskov, *Phys. Chem. Chem. Phys.* **2014**, *16*, 13156.

[20] Y. Liu, J. Wu, K. P. Hackenberg, J. Zhang, Y. M. Wang, Y. Yang, K. Keyshar, J. Gu, T. Ogitsu, R. Vajtai, J. Lou, P. M. Ajayan, B. C. Wood, B. I. Yakobson, *Nat. Energy* **2017**, *2*, 17127.

[21] J. Shi, X. Wang, S. Zhang, L. Xiao, Y. Huan, Y. Gong, Z. Zhang, Y. Li, X. Zhou, M. Hong, Q. Fang, Q. Zhang, X. Liu, L. Gu, Z. Liu, Y. Zhang, *Nat. Commun.* **2017**, *8*, 958.

[22] C. Tsai, K. Chan, J. K. Nørskov, F. Abild-Pedersen, *Surf. Sci.* **2015**, *640*, 133.

[23] H. Pan, *Sci. Rep.* **2015**, *4*, 5348.

[24] B. Han, S. H. Noh, D. Choi, M. H. Seo, J. Kang, J. Hwang, *J. Mater. Chem. A* **2018**, *6*, 20005.

[25] L. Najafi, S. Bellani, R. Oropesa-Nuñez, B. Martín-García, M. Prato, L. Pasquale, J.-K. Panda, P. Marvan, Z. Sofer, F. Bonaccorso, *ACS Catal.* **2020**, *10*, 3313.

[26] J. Zhang, J. Wu, X. Zou, K. Hackenberg, W. Zhou, W. Chen, J. Yuan, K. Keyshar, G. Gupta, A. Mohite, P. M. Ajayan, J. Lou, *Mater. Today* **2019**, *25*, 28.

[27] Y. Feng, K. Yu, Z. Zhu, *CrystEngComm* **2019**, *21*, 3517.

[28] D. N. Chirdon, Y. Wu, *Nat. Energy* **2017**, *2*, 17132.

[29] L. Najafi, S. Bellani, R. Oropesa-Nunez, B. Martín-García, M. Prato, V. Mazanek, D. Debellis, S. Lauciello, R. Brescia, Z. Sofer, F. Bonaccorso, *J. Mater. Chem. A* **2019**, *7*, 25593.

[30] J. Hwang, S. H. Noh, B. Han, *Appl. Surf. Sci.* **2019**, *471*, 545.

[31] C. Backes, C. Backes, A. M. Abdelkader, C. Alonso, A. Andrieux-Ledier, R. Arenal, J. Azpeitia, N. Balakrishnan, L. Banszerus, J. Barjon, R. Bartali, S. Bellani, C. Berger, R. Berger, M. M. Bernal Ortega, C. Bernard, P. H. Beton, A. Beyer, A. Bianco, P. Bøggild, F. Bonaccorso, G. Borin Barin, C. Botas, R. A. Bueno, D. Carriazo, A. Castellanos-Gomez, M. Christian, A. Ciesielski, T. Ciuk, M. T. Cole, J. Coleman, C. Coletti, L. Crema, H. Cun, D. Dasler, D. De Fazio, N. Díez, S. Drieschner, et al., *2D Mater.* **2020**, *7*, 022001.

[32] In order to avoid any cause of damage to previous works and companies, we purposely decide to not report any reference on this topic.

[33] *Preparation and Crystal Growth of Materials with Layered Structures*, Vol. *1* (Ed. R. M. A. Lieth), Springer Science & Business Media, Dordrecht, Netherlands **1977**.

[34] J. A. Wilson, F. J. Di Salvo, S. Mahajan, *Adv. Phys.* **1975**, *32*, 882.

[35] T. Shimada, F. S. Ohuchi, A. Koma, *Surf. Sci.* **1993**, *291*, 57.

[36] E. Figueroa, Y. K. Kuo, A. Olinger, M. A. Lloyd, L. D. Bastin, S. Petrotsatos, Q. Chen, B. Dobbs, S. Dev, J. P. Selegue, L. E. DeLong, C. P. Brock, J. W. Brill, *J. Solid State Chem.* **1995**, *114*, 486.

[37] S. F. Meyer, R. E. Howard, G. R. Stewart, J. V. Acrivos, T. H. Geballe, *J. Chem. Phys.* **1975**, *62*, 4411.

[38] A. R. Beal, *J. Phys. C: Solid State Phys.* **1978**, *11*, 4583.

[39] X. Chia, A. Ambrosi, P. Lazar, Z. Sofer, M. Pumera, *J. Mater. Chem. A* **2016**, *4*, 14241.

[40] K. Hayashi, A. Kawamura, *Mater. Res. Bull.* **1986**, *21*, 1405.

[41] J. Luxa, V. Mazánek, M. Pumera, P. Lazar, D. Sedmidubský, M. Callisti, T. Polcar, Z. Sofer, *Chem. Eur. J.* **2017**, *23*, 8082.

[42] F. Bonaccorso, A. Bartolotta, J. N. Coleman, C. Backes, *Adv. Mater.* **2016**, *28*, 6136.

[43] O. M. Maragó, F. Bonaccorso, R. Saija, G. Privitera, P. G. Gucciardi, M. A. Iatì, G. Calogero, P. H. Jones, F. Borghese, P. Denti, V. Nicolosi, A. C. Ferrari, *ACS Nano* **2010**, *4*, 7515.

[44] D. Dallinger, C. O. Kappe, *Chem. Rev.* **2007**, *107*, 2563.

[45] M. Q. Ning, M. M. Lu, J. B. Li, Z. Chen, Y. K. Dou, C. Z. Wang, F. Rehman, M. S. Cao, H. B. Jin, *Nanoscale* **2015**, *7*, 15734.

[46] D. Zhang, Y. Jia, J. Cheng, S. Chen, J. Chai, X. Yang, Z. Wu, H. Wang, W. Zhang, Z. Zhao, C. Han, M. Cao, G. P. Zheng, *J. Alloys Compd.* **2018**, *758*, 62.

[47] R. W. Sillars, *J. Inst. Electr. Eng. [1889-1940]* **1937**, *80*, 378.

[48] X. Liang, X. Zhang, W. Liu, D. Tang, B. Zhang, G. Ji, *J. Mater. Chem. C* **2016**, *4*, 6816.

[49] E. Hirota, *J. Phys. Chem.* **1979**, *83*, 1457.

[50] E. Navarro-Moratalla, J. O. Island, S. Mañas-Valero, E. Pinilla-Cienfuegos, A. Castellanos-Gomez, J. Quereda, G. Rubio-Bollinger, L. Chirolli, J. A. Silva-Guillén, N. Agraït, G. A. Steele, F. Guinea, H. S. J. van der Zant, E. Coronado, *Nat. Commun.* **2016**, *7*, 11043.

[51] Z. Zeng, C. Tan, X. Huang, S. Bao, H. Zhang, *Energy Environ. Sci.* **2014**, *7*, 797.

[52] A. V. Naumkin, A. Kraut-Vass, C. J. Powell, S. W. Gaarenstroom, NIST Standard Reference Database 20 version 4.1 **2012**.

[53] Z. Wang, Y. Y. Sun, I. Abdelwahab, L. Cao, W. Yu, H. Ju, J. Zhu, W. Fu, L. Chu, H. Xu, K. P. Loh, *ACS Nano* **2018**, *12*, 12619.

[54] R. Hovden, A. W. Tsen, P. Liu, B. H. Savitzky, I. E. l. Baggari, Y. Liu, W. Lu, Y. Sun, P. Kim, A. N. Pasupathy, L. F. Kourkoutis, *Proc. Natl. Acad. Sci. USA* **2016**, *113*, 11420.

[55] R. V. Gonçalves, R. Wojcieszak, P. M. Uberman, S. R. Teixeira, L. M. Rossi, *Phys. Chem. Chem. Phys.* **2014**, *16*, 5755.

[56] S. Hellmann, M. Beye, C. Sohrt, T. Rohwer, F. Sorgenfrei, H. Redlin, M. Kalläne, M. Marczynski-Bühlow, F. Hennies, M. Bauer, A. Föhlisch, L. Kipp, W. Wurth, K. Rossnagel, *Phys. Rev. Lett.* **2010**, *105*, 187401.

[57] M. Wahlqvist, A. Shchukarev, *J. Electron Spectrosc. Relat. Phenom.* **2007**, *156*, 310.

[58] K. Persson, P. Materials, Materials Data on TaS2 (SG:194) by Materials Project, United States **2015**, https://www.osti.gov/dataexplorer/biblio/dataset/1195033.

[59] J. C. H. Spence, *High-Resolution Electron Microscopy*, 4th ed., Oxford University Press, Oxford, UK, **2010**.

[60] M. Precner, T. Polakovič, Q. Qiao, D. J. Trainer, A. V. Putilov, C. Di Giorgio, I. Cone, Y. Zhu, X. X. Xi, M. Iavarone, G. Karapetrov, *Sci. Rep.* **2018**, *8*, 6724.

[61] J. Chen, S. Zhou, Y. Wen, G. H. Ryu, C. Allen, Y. Lu, A. I. Kirkland, J. H. Warner, *Nanoscale* **2019**, *11*, 1901.

[62] H.-P. Komsa, S. Kurasch, O. Lehtinen, U. Kaiser, A. V. Krasheninnikov, *Phys. Rev. B* **2013**, *88*, 35301.

[63] A. Azizi, X. Zou, P. Ercius, Z. Zhang, A. L. Elías, N. Perea-López, G. Stone, M. Terrones, B. I. Yakobson, N. Alem, *Nat. Commun.* **2014**, *5*, 4867.

[64] J. Lin, S. T. Pantelides, W. Zhou, *ACS Nano* **2015**, *9*, 5189.

[65] L. Najafi, S. Bellani, R. Oropesa-Nuñez, A. Ansaldo, M. Prato, A. E. Del Rio Castillo, F. Bonaccorso, *Adv. Energy Mater.* **2018**, *8*, 1801764.

[66] B. Martín-García, D. Spirito, S. Bellani, M. Prato, V. Romano, A. Polovitsyn, R. Brescia, R. Oropesa-Nuñez, L. Najafi, A. Ansaldo, G. D'Angelo, V. Pellegrini, R. Krahne, I. Moreels, F. Bonaccorso, *Small* **2019**, *15*, 1904670.

[67] F. Xi, P. Bogdanoff, K. Harbauer, P. Plate, C. Höhn, J. Rappich, B. Wang, X. Han, R. van de Krol, S. Fiechter, *ACS Catal.* **2019**, *9*, 2368.

[68] S. Anantharaj, S. R. Ede, K. Karthick, S. Sam Sankar, K. Sangeetha, P. E. Karthik, S. Kundu, *Energy Environ. Sci.* **2018**, *11*, 744.

[69] C. C. L. McCrory, S. Jung, J. C. Peters, T. F. Jaramillo, *J. Am. Chem. Soc.* **2013**, *135*, 16977.

[70] S. Trasatti, O. A. Petrii, *J. Electroanal. Chem.* **1992**, *327*, 353.

[71] C. Greenhow, W. V. Smith, *J. Chem. Phys.* **1951**, *19*, 1298.

[72] I. M. K. Ismail, *Langmuir* **1992**, *8*, 360.

[73] K. Tang, X. Wang, Q. Li, C. Yan, *Adv. Mater.* **2018**, *30*, 1704779.

[74] J. Yang, A. R. Mohmad, Y. Wang, R. Fullon, X. Song, F. Zhao, I. Bozkurt, M. Augustin, E. J. G. Santos, H. S. Shin, W. Zhang, D. Voiry, H. Y. Jeong, M. Chhowalla, *Nat. Mater.* **2019**, *18*, 1309.

[75] J. Zhang, Y. Zhao, X. Guo, C. Chen, C. L. Dong, R. S. Liu, C. P. Han, Y. Li, Y. Gogotsi, G. Wang, *Nat. Catal.* **2018**, *1*, 985.

[76] L. Najafi, S. Bellani, A. Castelli, M. P. Arciniegas, R. Brescia, R. Oropesa-Nuñez, B. Martín-García, M. Serri, F. Drago, L. Manna, F. Bonaccorso, *Chem. Mater.* **2020**, *32*, 2420.

[77] N. Cheng, S. Stambula, D. Wang, M. N. Banis, J. Liu, A. Riese, B. Xiao, R. Li, T. K. Sham, L. M. Liu, G. A. Botton, X. Sun, *Nat. Commun.* **2016**, *7*, 13638.

[78] J. Deng, H. Li, J. Xiao, Y. Tu, D. Deng, H. Yang, H. Tian, J. Li, P. Ren, X. Bao, *Energy Environ. Sci.* **2015**, *8*, 1594.

[79] H. Zhang, P. An, W. Zhou, B. Y. Guan, P. Zhang, J. Dong, X. W. Lou, *Sci. Adv.* **2018**, *4*, 6657.

[80] X. Cheng, Y. Li, L. Zheng, Y. Yan, Y. Zhang, G. Chen, S. Sun, J. Zhang, *Energy Environ. Sci.* **2017**, *10*, 2450.

[81] L. Zhang, L. Han, H. Liu, X. Liu, J. Luo, *Angew. Chem., Int. Ed.* **2017**, *56*, 13694.

[82] A. H. Ghanim, J. G. Koonce, B. Hasa, A. M. Rassoolkhani, W. Cheng, D. W. Peate, J. Lee, S. Mubeen, *Front. Chem.* **2018**, *6*, 523.

[83] H. Tian, X. Cui, L. Zeng, L. Su, Y. Song, J. Shi, *J. Mater. Chem. A* **2019**, *7*, 6285.

[84] A. Jagminas, A. Naujokaitis, R. Žalneravičius, V. Jasulaitiene, G. Valušis, *Appl. Surf. Sci.* **2016**, *385*, 56.

[85] C. Kittel, *Introduction to Solid State Physics*, 8th ed., John Wiley & Sons, New York, NY **2004**.

[86] E. Roduner, *Chem. Soc. Rev.* **2006**, *35*, 583.

[87] J. K. Nørskov, T. Bligaard, A. Logadottir, J. R. Kitchin, J. G. Chen, S. Pandelov, U. Stimming, *J. Electrochem. Soc.* **2005**, *152*, J23.

[88] Y. H. Fang, Z. P. Liu, *ACS Catal.* **2014**, *4*, 4364.